PAPER

Check for updates

Sustaining vacancy catalysis *via* conformal graphene overlays boosts practical Li–S batteries†

Jiaxi Gu,‡[a] Zixiong Shi,‡[b] Yongbiao Mu,‡[c] Yuzhu Wu,‡[d] Meng Tian, [ID] *[e] Ziang Chen,[a] Kaihui Chen,[e] Huicun Gu,[c] Miaoyu Lu,[a] Lin Zeng, [ID] *[c] Yuqing Song,*[d] Qiang Zhang [ID] [f] and Jingyu Sun [ID] *[ad]

Sluggish reaction kinetics and uncontrollable dendrite growth are deemed as the main bottlenecks for practical Li–S batteries. Notwithstanding fruitful advances in designing dual-functional mediators for both electrodes, cooperative efforts on protecting catalytically active sites and optimizing solid electrolyte interphase (SEI) by the employment of industrial catalysts are still lacking. Herein, an oxygen vacancy (V_O)-sustained prototype mediator with layer-number controllable graphene modification (Al_2O_3@mG) is developed for concurrently accelerating redox kinetics at the S cathode and harvesting inorganic-rich SEI at the Li anode. Theoretical and experimental analyses reveal that V_O enhances the electrocatalytic activity while the graphene overlay serving as a catalysis sustainer enables vacancy protection. Meanwhile, Al_2O_3@mG is conducive to homogenizing Li-ion flux and boosting preferential decomposition of anions, thereby stabilizing the Li metal anode. Benefiting from such dual-functional reformulation, Li–S batteries with Al_2O_3@mG modified separators achieve a low capacity decay of 0.032% per cycle over 1600 cycles at 1.0 C. The assembled pouch cell delivers high areal capacity and stable cycling operation. Such a vacancy-sustained graphene strategy showcases promising universality to be applied on various oxide candidates, offering meaningful guidance in mediator design toward pragmatic Li–S batteries.

Broader context

Lithium–sulfur (Li–S) batteries stand out as one of the most promising energy storage systems owing to their energy density (2600 Wh kg^{-1}), cost effectiveness, and environmentally friendly nature. The key issues impeding their development lie in severe polysulfide crossover and uncontrollable dendrite growth, which impose considerable limitations on the cycling lifetime of Li–S batteries. Dual-functional mediators have been widely investigated as a potential solution strategy. However, cooperative efforts on protecting catalytically active sites and optimizing solid electrolyte interphase (SEI) are still lacking. In this study, an oxygen vacancy (V_O)-sustained Al_2O_3 prototype mediator with layer-number controllable graphene modification (Al_2O_3@mG) is developed for concurrently accelerating redox kinetics at the sulfur cathode and harvesting inorganic-rich SEI at the lithium anode. V_O enhances the electrocatalytic activity of Al_2O_3 while the graphene overlay serving as a catalysis sustainer enables vacancy protection. Meanwhile, Al_2O_3@mG is conducive to homogenizing Li-ion flux and boosting the preferential decomposition of anions, thereby stabilizing the Li metal anode. This work delineates a vacancy-sustained graphene strategy, which showcases promising universality for application in various oxide candidates and further offering meaningful guidance to design dual-functional mediators toward pragmatic Li–S batteries.

[a] *College of Energy, Soochow Institute for Energy and Materials Innovations, Key Laboratory for Advanced Carbon Materials and Wearable Energy Technologies of Jiangsu Province, Soochow University, Suzhou 215006, China. E-mail: sunjy86@suda.edu.cn*

[b] *Materials Science and Engineering, Physical Science and Engineering Division, King Abdullah University of Science and Technology, Thuwal 23955-6900, Saudi Arabia*

[c] *Shenzhen Key Laboratory of Advanced Energy Storage, Department of Mechanical and Energy Engineering, Southern University of Science and Technology, Shenzhen 518055, China. E-mail: zengl3@sustech.edu.cn*

[d] *Beijing Graphene Institute, Beijing 100095, China. E-mail: songyq@bgi-graphene.com*

[e] *School of New Energy, School of Intelligent Manufacturing, Nanjing University of Science and Technology, Jiangyin 214443, China. E-mail: tianmeng@njust.edu.cn*

[f] *Department of Chemical Engineering, Tsinghua University, Beijing 100084, China*

† Electronic supplementary information (ESI) available. See DOI: https://doi.org/10.1039/d5ee01134e

‡ These authors contributed equally to this work.

This journal is © The Royal Society of Chemistry 2025

Introduction

Lithium–sulfur (Li–S) batteries have received extensive research attention in response to the growing demand for next-generation energy storage systems.[1–5] The key issues impeding their development lie in severe polysulfide crossover and uncontrollable dendrite growth, which impose considerable limitations on the cycling lifetime, especially under harsh conditions such as elevated sulfur loading and large current density.[6–10] Recent years have witnessed the appearance of a "one bird two stone" strategy to devise effective mediators with dual sulfiphilicity and lithiophilicity, simultaneously enabling facile sulfur redox kinetics and homogeneous lithium metal deposition.[11–15]

To achieve boosted sulfur redox reaction and suppressed "shuttling effect", a myriad of mediators with strong electrocatalytic effect have been developed, where vacancy engineering is regarded as a crucial solution to augmenting active sites.[16–20] Despite enhanced catalytic activity for sulfur cathodes, insulating discharge products (i.e., Li_2S_2/Li_2S) are prone to deposit over the limited catalyst surfaces without sufficient decomposition, hence the active sites are continuously deteriorated.[21,22] In this case, it is anticipated that vacancies are vulnerable to various electronegative sulfur species, which would exacerbate the detrimental coverage on active sites along with severe accumulation of "dead" sulfides. Although such a catalyst failure has been identified as a universal phenomenon in the aprotic environment of Li–S batteries, strategies for sustaining the active sites are still lacking. Our recent endeavours unravelled that grown graphene coatings effectively armor the electrocatalysts, whereby both the catalytic activity and durability were elevated.[23–25] Nevertheless, the strategic feasibility in protecting vacancy-rich electrocatalysts has not been explored. In this respect, it is imperative to decipher the function mechanism and actual sustainability of vacancies under the shielding of graphene chainmail.

In parallel, whether vacancy engineering would exert positive effects on stabilizing the Li metal anode is still questionable, wherein the fundamental understanding of the vacancy-mediated electrolyte decomposition pathway and chemical component distribution in as-formed solid electrolyte interphase (SEI) would be a key. Meanwhile, exploring the synergistic effect between vacancies and graphene on rendering a stable Li metal anode is also highly desirable. Inspired by these considerations, prevailing industrial catalyst Al_2O_3 is employed as a prototype dual-functional mediator, where oxygen vacancies (V_O) are constructed during the chemical vapor deposition (CVD)-derived graphene growth process. Throughout the delicate thickness adjustment of graphene coatings, few-layer, multi-layer or thick-layer graphene is customized onto powdery Al_2O_3 (denoted as Al_2O_3@fG, Al_2O_3@mG and Al_2O_3@tG) with the aim to concurrently accelerate sulfur reaction kinetics and afford inorganic-rich SEI for long-life Li–S batteries (Fig. 1a). In one case, electrocatalytic activity of Al_2O_3 could be boosted with V_O introduction. The multi-layer graphene armor can serve as a vacancy catalysis sustainer to mitigate the detrimental coverage of discharge products and restrain the "poisoning" of

active sites. In another case, V_O is beneficial for inducing homogenous Li deposition and promoting the preferential decomposition of anions, thereby generating and maintaining inorganic-rich SEI to suppress the dendritic growth at the anode side. Benefiting from such a dual-functional mediator effect, Li–S batteries equipped with Al_2O_3@mG modified separators harvest an initial capacity of 1307.5 mA h g^{-1} at 0.2 C, accompanied by a negligible fading rate of 0.032% for 1600 cycles at 1.0 C. The assembled pouch cell delivers an impressive areal capacity of 5.3 mA h cm^{-2}, accompanied by a reasonable lifespan over 70 cycles. This strategy shows an appealing universality, which could be extended to other oxide catalysts (MgO, TiO_2, and MoO_3). Our work reveals the vital merits of synergistic vacancy engineering and graphene armoring for the optimization of interfacial electrochemistry, which affords practical insight into the rational design of advanced mediators for Li–S batteries.

Results and discussion

Vacancy-sustained graphene design

The Al_2O_3@G with varied layer numbers of graphene coating was achieved via a well-designed direct CVD synthesis. First, an Ar flow (100 sccm) was introduced into the furnace at room temperature while it was gradually increased to 1100 °C, followed by a preliminary treatment for 10 min with a H_2 flow (50 sccm) to remove surface contaminants of Al_2O_3. Subsequently, CH_4 (10 sccm) serves as the carbon precursor to enable controllable graphene growth under a mixed gas flow of H_2 (50 sccm) and Ar (100 sccm), thus deriving Al_2O_3@G with a high production yield (Fig. 1b). It is worth noting that the layer number of the graphene shell can be tuned by altering the reaction duration. Likewise, TiO_2@G, MgO@G and MoO_3@G could be synthesized by changing the growth supports.

X-ray diffraction (XRD) was utilized to probe the crystal phases of as-synthesized Al_2O_3@G. As illustrated in Fig. S1 (ESI†), the predominant signals of all samples match well with the (012) and (113) planes of α-Al_2O_3.[26] Raman spectra were recorded to investigate the structural features of graphene. As shown in Fig. 1c, the typical peaks of the D band (1335 cm^{-1}), G band (1570 cm^{-1}) and 2D band (2668 cm^{-1}) can be detected, corroborating graphene formation.[27,28] Meanwhile, electron paramagnetic resonance (EPR) profiles were collected to gain insight into the defect characteristics. In this respect, distinct EPR signals that can be observed at a g-value of 2.003 for Al_2O_3@G are missing for pure Al_2O_3 (Fig. 1d and Fig. S2, ESI†), which is attributed to the partial removal of O atoms to generate unpaired electrons.[29] This verifies the successful introduction of V_O under thermal treatment with a reducing atmosphere. Notably, the concentration of V_O is boosted with the extension of the CVD growth time, which might play a role in modulating the electrocatalytic activity of Al_2O_3.

The morphologies of Al_2O_3@G were inspected by scanning electron microscopy (SEM) and transmission electron microscopy (TEM). Upon graphene coating, there is no discernible

This journal is © The Royal Society of Chemistry 2025

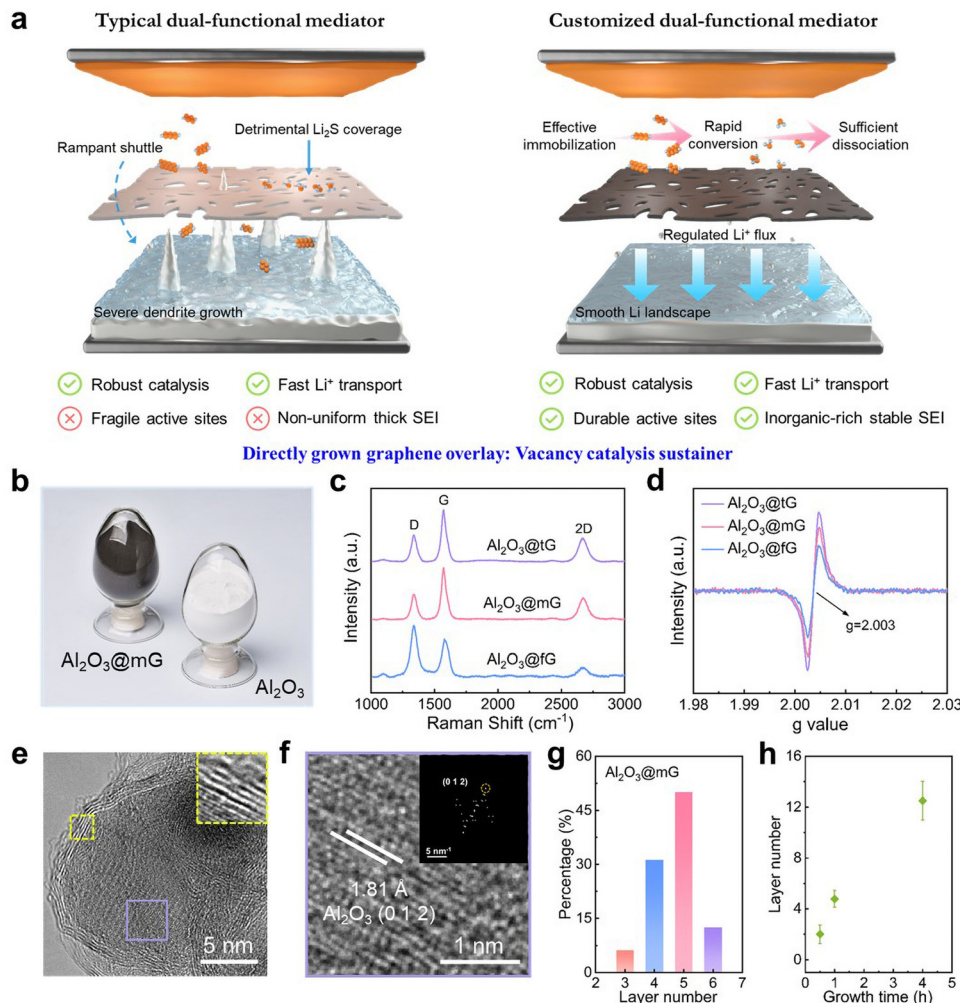*Energy Environ. Sci.*, 2025, **18**, 5940–5951 | **5941**

Fig. 1 Vacancy-sustained graphene design. (a) Schematic illustrating the comparison between conventional dual-functional mediators and our strategic design for Li–S full batteries. (b) Digital photo of Al_2O_3@mG with a high yield. (c) Raman spectra of Al_2O_3@fG, Al_2O_3@mG and Al_2O_3@tG. (d) EPR spectra of Al_2O_3@fG, Al_2O_3@mG and Al_2O_3@tG. (e) TEM image of Al_2O_3@mG. Inset: HRTEM image of the graphene overlay. (f) HRTEM image of Al_2O_3@mG. Inset: Corresponding FFT pattern. (g) Statistical analysis of the graphene layer number for Al_2O_3@mG. (h) The relationship between the layer number and growth time of the graphene overlay.

difference in powdery morphology between bare Al_2O_3 and Al_2O_3@G (Fig. S3, ESI†). As shown in high-resolution TEM (HRTEM) images of Al_2O_3@mG, Al_2O_3@fG and Al_2O_3@tG (Fig. 1e and Fig. S4, ESI†), a lattice spacing of 1.81 Å for the inner core area could be clearly identified (Fig. 1f), corresponding to the (012) plane of α-Al_2O_3 *via* the fast Fourier transform (FFT) pattern.[30] Statistical analysis of the HRTEM images shows that the graphene shells grown on the Al_2O_3 core can be dictated at 4–6 layers (Fig. 1g and Fig. S5, ESI†), which is anticipated to achieve a balance between activity and stability for polysulfide electrocatalysis. Furthermore, the graphene shells of Al_2O_3@fG and Al_2O_3@tG are respectively adjusted to *ca.* 2 and 12 layers (Fig. 1h), again confirming the precise regulation of the layer numbers *via* our direct CVD route. The good tunability of the graphene overlay would help elucidate the evolution of vacancy-rich catalysts during the polysulfide conversion reaction. Energy-dispersive X-ray analysis of Al_2O_3@mG reveals the homogeneous element distribution

(Fig. S6, ESI†), indicative of uniform graphene encapsulation over the inner Al_2O_3 core.

Polysulfide adsorption and catalytic conversion

To unravel the merits of V_O-rich Al_2O_3 with tunable graphene chainmail in promoting bidirectional sulfur chemistry, a series of electro-kinetic analysis was performed.[31] It is well accepted that both Li_2S nucleation and dissociation afford a considerable energy barrier, which were investigated by potentiostatic intermittent titration technique (PITT) measurement.[32] As for Li_2S nucleation, the assembled battery was potentiostatically discharged from 2.25 to 1.90 V with an interval of 50 mV (Fig. 2a). The current peaks at 2.0 V are ascribed to Li_2S precipitation from soluble polysulfide intermediates, wherein Al_2O_3@mG shows the highest peak intensity and the earliest time to reach the peak as compared to its counterparts (Fig. S7, ESI†). As manifested in Fig. 2b, the Al_2O_3@mG exhibits the largest capacity (194.3 mA h g_s^{-1}). In parallel, Li_2S dissociation

5942 | *Energy Environ. Sci.*, 2025, **18**, 5940–5951

This journal is © The Royal Society of Chemistry 2025

was investigated by potentiostatically charging the batteries from 2.20 to 2.50 V, with each interval of 100 mV, in which Al$_2$O$_3$@mG also displays the highest current response and fastest reaction kinetics (Fig. S8, ESI†). These results suggest that Al$_2$O$_3$@mG harnesses electrocatalytic robustness for expediting dual-directional sulfur redox reaction. *In situ* Raman probing of the Li–S cell with Al$_2$O$_3$@mG/PP was performed during a complete discharge/charge cycle, where the dynamic changes of LiPS speciation and concentration could be tracked. As indicated in Fig. S9 (ESI†), a gradual weakening of polysulfide signals including S$_8^{2-}$, S$_6^{2-}$ and S$_3^{2-}$ can be observed during the discharging process, followed by a continuous signal enhancement during the subsequent charging, indicative of kinetically favorable LiPS conversion. Cyclic voltammetry (CV) profiles of the symmetric cells were collected in a Li$_2$S$_6$-containing electrolyte at a scan rate of 50 mV s^{-1}. Apparently, Al$_2$O$_3$@mG enables the highest redox current response with improved reversibility (Fig. 2c and Fig. S10, ESI†). Meanwhile, it also harvests sharper and stronger redox peaks as compared to its counterparts at a scan rate of 0.5 mV s^{-1}, suggestive of

boosted electrocatalytic activity for polysulfide conversion (Fig. 2d and e and Fig. S11, ESI†). In this respect, other metal oxide catalysts also display strong electrocatalytic capability (Fig. S12, ESI†), manifesting that our graphene overlayer as a vacancy sustainer is widely applicable for electrocatalyst modification.

Since optimized adsorption capability plays a vital role in mitigating the LiPS shuttle, the visualized Li$_2$S$_6$ adsorption test was carried out (Fig. S13, ESI†). Upon the addition of Al$_2$O$_3$@mG, the Li$_2$S$_6$ solution was rapidly decoloured, suggesting the efficient restriction of LiPS dissolution/diffusion. With respect to the UV-Vis spectroscopic study, the Li$_2$S$_6$ solution mixed with the Al$_2$O$_3$@mG exhibits the weakest absorption peak, further implying its strong polysulfide adsorption ability on account of V$_O$ sites. To further explore the synergistic effect of vacancy engineering and graphene armoring on propelling sulfur redox kinetics, density functional theory (DFT) calculation was performed. The crystal orbital Hamilton population (COHP) was employed to describe the orbital–pair interactions. As depicted in Fig. S14 (ESI†), three catalyst configurations are
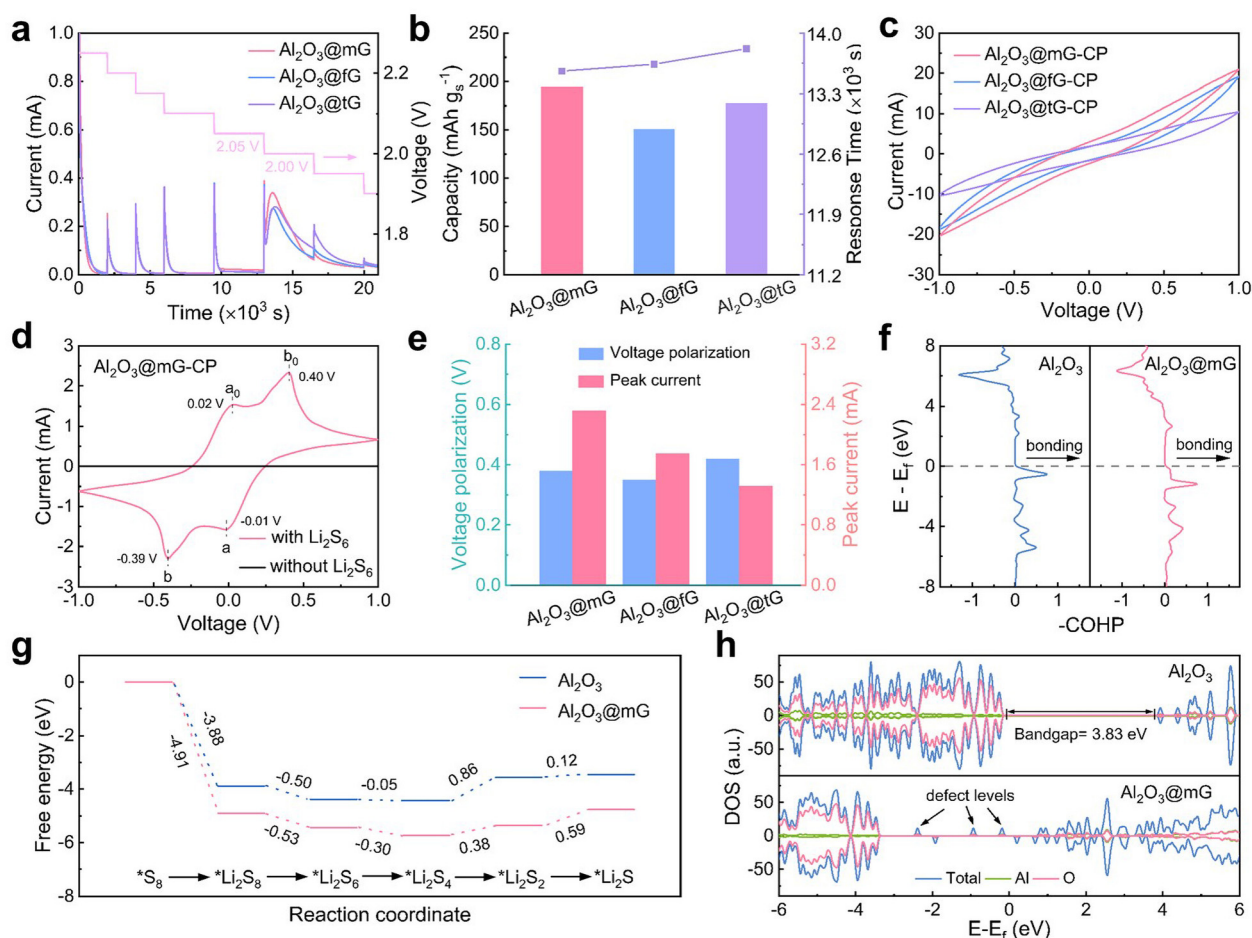

Fig. 2 Adsorption and catalytic conversion of polysulfides. (a) Current–time profiles and (b) corresponding response time and calculated capacity in the PITT discharging test. (c) CV curves of Al$_2$O$_3$@fG-CP, Al$_2$O$_3$@mG-CP and Al$_2$O$_3$@tG-CP symmetric cells at a scan rate of 50 mV s^{-1}. (d) CV curves of Al$_2$O$_3$@mG-CP symmetric cell at 0.5 mV s^{-1}. (e) Comparison of the voltage polarization and peak current for Al$_2$O$_3$@G samples. (f) COHP of Al–S bond. (g) Calculated Gibbs free energy for the stepwise sulfur reduction reaction on Al$_2$O$_3$ and Al$_2$O$_3$@mG. (h) DOS profiles showing the charge density of Al$_2$O$_3$ and Al$_2$O$_3$@mG.

included: Al_2O_3, Al_2O_3 with single oxygen vacancy (Al_2O_{3-x}) and Al_2O_3 with double oxygen vacancies (Al_2O_{3-2x}). The results show that the adsorption energy of Li_2S_2 increased with the introduction of V_O, in accordance with the integrated crystal orbital Hamilton population (–ICOHP) analysis. In the meantime, a similar trend can be observed with respect to the Al–S bond between $Al_2O_3@G$ and Li_2S_4, demonstrative of enhanced polysulfide immobilization (Fig. S15, ESI†).[33] Additionally, COHP was employed to resolve the states of the metal–sulfur bond, wherein the positive and negative COHP represent the bonding and anti-bonding contribution, respectively.[34] Since fewer occupied electrons in the anti-bonding orbital represent stronger metal–sulfur interaction, $Al_2O_3@G$ possesses a stronger Al–S bond for enhancing Li_2S_4 adsorption (Fig. 2f). Gibbs free energy change (ΔG) for multi-step sulfur reduction reactions was further calculated (Fig. 2g and Fig. S16 and S17, ESI†). Notably, $Al_2O_3@G$ shows an apparently lower ΔG value than that of pristine Al_2O_3 for each step, indicative of promoted reaction kinetics. To investigate the underlying reasons, the electronic structure modification of the metal centre with the introduction of V_O was analysed based on the density of states (DOS). As shown in Fig. 2h and Fig. S18 (ESI†), V_O could introduce the defect levels, thereby narrowing the width of the band-gap. Consequently, it facilitates electron transfer from Al to S atoms and strengthens the Al–S hybridization bonding.

Li_2S dissociation pathways on Al_2O_3 with/without vacancy were modelled (Fig. S19 and S20, ESI†). As such, the lower energy barrier for $Al_2O_3@G$ implies higher reaction activity for the promotion of Li_2S decomposition.

Mechanism of active site failure and protection

To gain in-depth insight into the failure mechanism of $Al_2O_3@G$, *ex situ* EPR profiles were recorded. As shown in Fig. S21 (ESI†), the EPR intensities of both $Al_2O_3@fG$ and $Al_2O_3@tG$ exhibit an obvious decrease upon the discharge process, which might be attributed to the heavy deposition of discharge products without sufficient decomposition. In contrast, the EPR intensity of $Al_2O_3@mG$ displays a negligible change after electrochemical cycling (Fig. 3a and b). In this sense, the vacancy retention rate of $Al_2O_3@mG$ after 60 cycles at 1.0 C was derived to be 94.3%, which is higher than those of $Al_2O_3@fG$ (75.4%) and $Al_2O_3@tG$ (86.1%) (Fig. 3c). It is hence conjectured that the active sites of V_O can be well maintained in the presence of graphene armor with an optimized thickness. To further verify the protective effect of graphene on catalytic activity, CV profiles were continuously collected at a scan rate of 50 mV s^{-1}. As depicted in Fig. S22a (ESI†), $Al_2O_3@mG$ can still exhibit a high redox current response with favourable reversibility after 30 cycles, suggestive of a sustainable electrocatalytic activity. Meanwhile, Li–S batteries equipped with Al_2O_3-modified separators display an
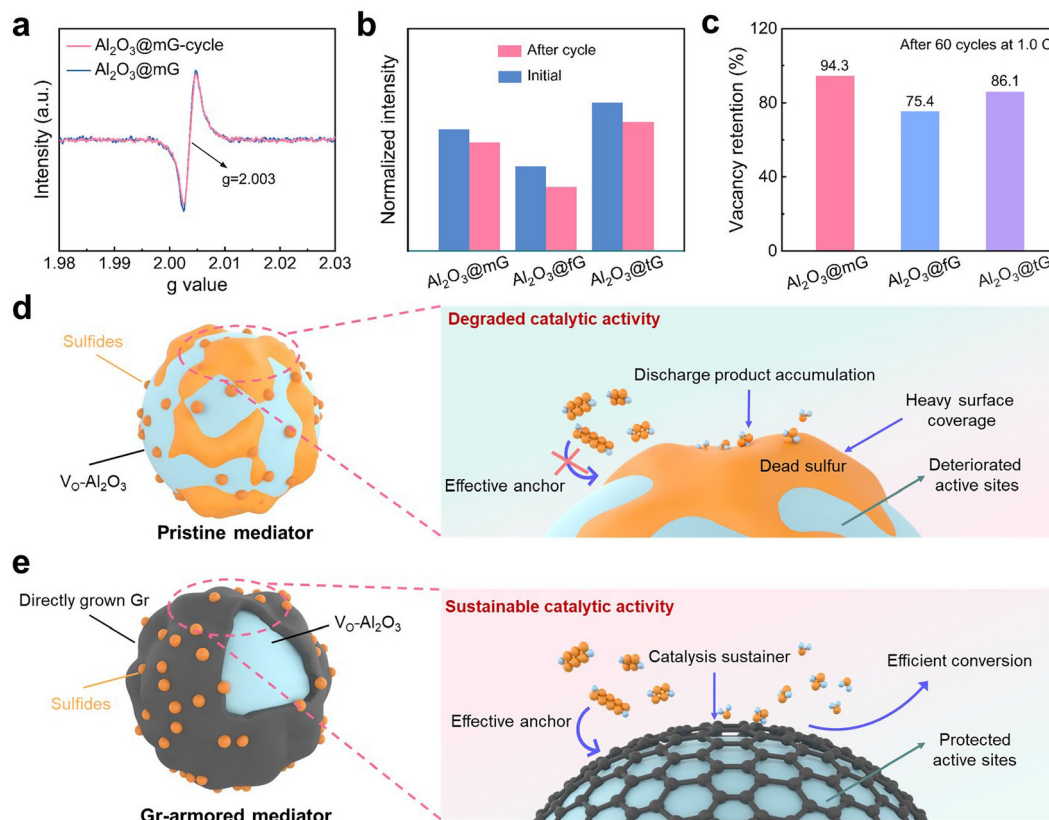

Fig. 3 Mechanism of active site failure and protection. (a) *Ex situ* EPR spectra of $Al_2O_3@mG$. (b) EPR intensity of different $Al_2O_3@G$ samples before and after cycling. (c) Corresponding vacancy retention rates after 60 cycles at 1.0 C. Schematic illustrating the evolution of vacancy sites on (d) the pristine mediator and (e) the graphene-armored mediator during the electrochemical process.
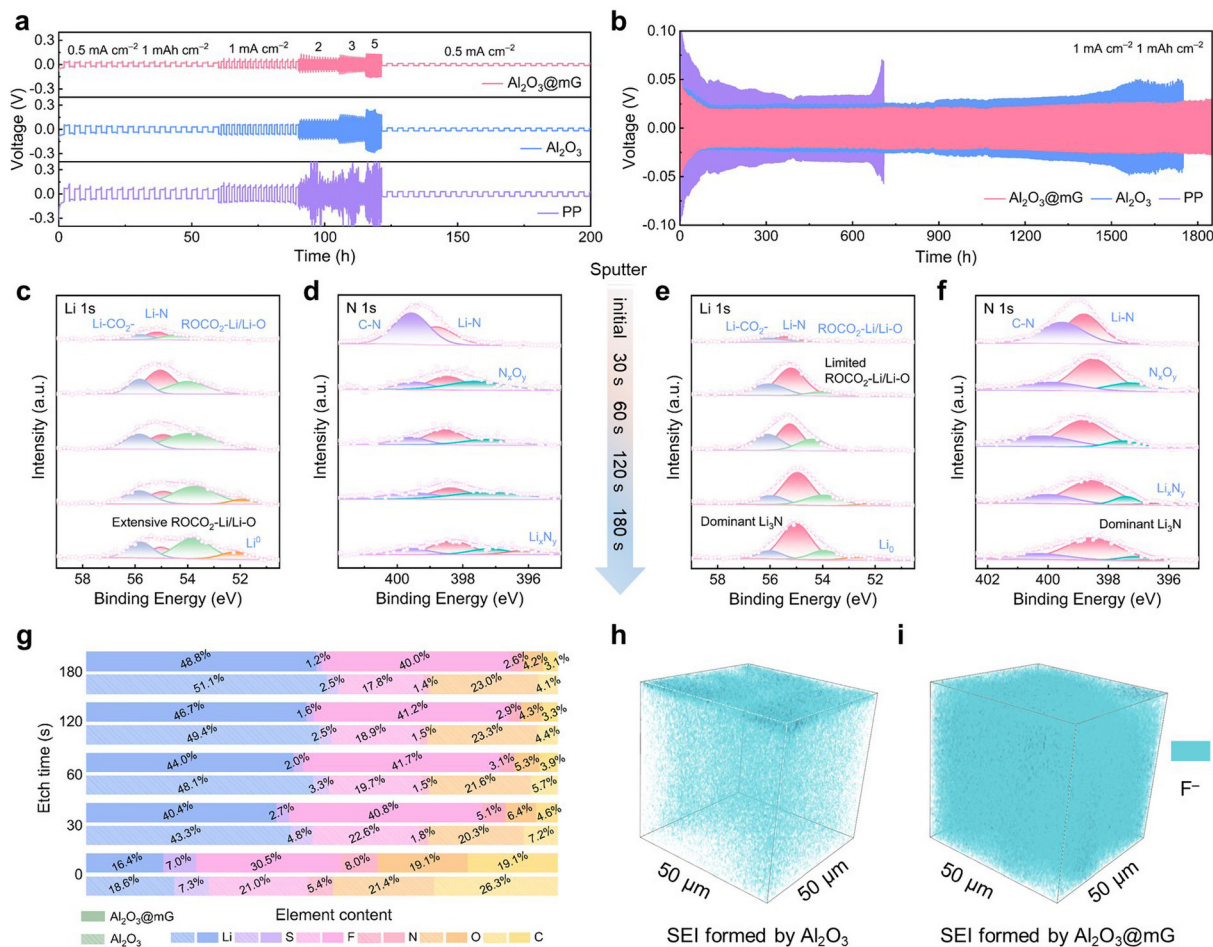
5944 | *Energy Environ. Sci.*, 2025, **18**, 5940–5951

This journal is © The Royal Society of Chemistry 2025

Fig. 4 Compositional analysis and mechanistic investigation of SEI. (a) Voltage–time profiles of Li||Li symmetric cells with Al_2O_3@mG/PP, Al_2O_3/PP and PP separators at a current density of 0.5, 1.0, 2.0, 3.0 and 5.0 mA cm^{-2} with a capacity of 1.0 mA h cm^{-2}. (b) Cycling performances at 1.0 mA cm^{-2}/ 1.0 mA h cm^{-2}. XPS depth profiling of (c and e) Li 1s and (d and f) N 1s spectra for (c and d) Al_2O_3 and (e and f) Al_2O_3@mG at different sputtering times. (g) Atomic concentrations at different etching depths. 3D reconstruction of the measured ToF-SIMS signal for F$^-$ secondary ion in the SEI formed via (h) Al_2O_3 and (i) Al_2O_3@mG.

apparent capacity decrease after resting for 20 h (Fig. S22b, ESI†). In stark contrast, Al_2O_3@mG/PP exhibits a negligible capacity loss (30.4 mA h g^{-1}), indicating a durable electrocatalytic effect to mitigate an irreversible loss of active species. The conspicuous advantages of multi-layer graphene overlay are demonstrated in Fig. S22c (ESI†). Molecular dynamics simulation based on the large-scale atomic/molecular massively parallel simulator was also carried out to probe the structural features of V_O.[35] With respect to Al_2O_{3-x} substrates with the aid of a graphene sustainer, V_O exhibits more stable states than that of bare Al_2O_{3-x} (Fig. S23, ESI†). Moreover, higher vacancy durability can be obtained when increasing the layer amount of graphene from one to three, suggesting that graphene chainmail can protect vacancy sites from "poisoning". Collectively, one can conclude that Al_2O_3@fG with a thin graphene coating suffers from an insufficient shielding effect toward V_O, whereas Al_2O_3@tG with thick layers hinders the complete release of the inner active sites. Both would lead to a rapid failure of active sites upon electrochemical reaction (Fig. 3d). The direct-CVD-enabled graphene with moderate thickness serves as a sustainer to protect vacancy sites,

which is conducive to mitigating the detrimental coverage of discharge product while facilitating dual-directional sulfur redox (Fig. 3e).

SEI compositional analysis and mechanistic investigation

To evaluate the impact of Al_2O_3@G on the lithium metal anode, Li||Li symmetric cell tests employing a PP separator were first carried out.[36] Rate performances of Al_2O_3@mG/PP, Al_2O_3@fG/ PP, Al_2O_3@tG/PP, Al_2O_3/PP, and PP were recorded under different current densities from 0.5 to 5.0 mA cm^{-2} with a fixed capacity of 1.0 mA h cm^{-2} (Fig. 4a and Fig. S24, ESI†). The cell with Al_2O_3@mG/PP delivers the lowest overpotential as well as the smallest voltage fluctuation. With respect to the Li plating/ stripping test at 1.0 mA cm^{-2}/1.0 mA h cm^{-2}, Al_2O_3@mG/PP displays a superior cycling stability over 1800 h with a low voltage polarization while bare PP suffers from premature failure (Fig. 4b and Fig. S25 and S26, ESI†). Impressively, the cycling performance of Al_2O_3@mG/PP compares favourably with other advanced separator designs in Li–S batteries (Table S1, ESI†).[12,13,17,36–40] Furthermore, deposited Li metal with V_O-

This journal is © The Royal Society of Chemistry 2025

Energy Environ. Sci., 2025, 18, 5940–5951 | 5945

Al_2O_3@mG/PP exhibits a smoother morphology than its other counterparts after cycling, demonstrative of its key role in stabilizing the Li metal anode (Fig. S27, ESI†). As shown in Fig. S28 (ESI†), the voltage curve of the Li||Cu cell with the Al_2O_3@mG/Cu electrode also exhibits a smaller nucleation overpotential of 30.1 mV in comparison with that of Al_2O_3@fG/Cu (39.8 mV), Al_2O_3@tG/Cu (44.9 mV), Al_2O_3/Cu (48.3 mV), and bare Cu (75.9 mV). In addition, a high average Coulombic efficiency (CE) over 98.5% can be obtained on the Al_2O_3@mG/Cu electrode, indicative of its favourable lithiophilicity for homogeneous Li metal deposition.

It is well established that the chemical components of SEI help govern the ion transport and interfacial stability at the anode/electrolyte interface.[38,41,42] To investigate the roles of vacancy engineering in modulating SEI's composition, XPS depth profiling of the cycled Li metal anode was carried out. As for the Li 1s spectrum, three peaks appearing at 56.1, 55.2 and 54.0 eV respectively correspond to $Li-CO_3^{2-}$, Li–N, and $ROCO_2-Li/Li-O$ (Fig. 4c and e).[43] Two deconvoluted signals at 399.6 and 398.8 eV in the N 1s spectrum are ascribed to C–N and Li–N bonds, respectively (Fig. 4d and f).[44] In the F 1s profile, C–F (688.8 eV) and Li–F (685.2 eV) bonds could be identified (Fig. S29, ESI†).[45] Notably, the existence of $ROCO_2-Li/Li-O$ and C–F bonds indicates the formation of organic species from solvent decomposition, while the inorganic components (*e.g.*, Li_2CO_3, Li_3N and LiF) are usually derived from TFSI anions.[46] With the increase of etching time, the proportion of $ROCO_2-Li/Li-O$ species formed *via* bare Al_2O_3 is gradually augmented. Even after Ar^+ etching for 180 s, organic components still exhibit an overwhelming advantage, which is detrimental to Li-ion transportation and interfacial stability. Encouragingly, massive inorganic components exist in the SEI formed by Al_2O_3@mG, wherein the percentages of Li_3N and LiF remain continuously high at different etching states. Upon Ar^+ etching treatment, Li_3N and LiF signals in the SEI layer are continuously increased for the Al_2O_3@mG electrode, which are stabilized at 60 s and become the dominant inorganic components. At 120 s of etching time, the ratio of N and F elements is almost twice as high as that formed by bare Al_2O_3 (Fig. S30, ESI†), again verifying the formation of an inorganic-rich SEI architecture under the regulation of V_O and graphene armor. Fig. 4g displays the elemental ratio distribution at different etching stages, where a high ratio of inorganic to organic species can be observed for the SEI generated by Al_2O_3@mG (Fig. S31, ESI†). The spatial distribution of N and F elements on the Li metal anode was further analysed by time-of-flight secondary ion mass spectrometry (ToF-SIMS). By investigating the secondary ion F^- and N^-, the 3D spatial distribution of LiF and Li_3N components can be unveiled.[47] The F^- intensity of Al_2O_3@mG is higher either on the surface or in the bulk than that for bare Al_2O_3 (Fig. 4h and i). In the meantime, a similar trend can be observed with respect to the distribution of N^- (Fig. S32, ESI†). It is therefore concluded that the presence of V_O promotes the formation of inorganic SEI constituents, thereby achieving a higher proportion of LiF and Li_3N. Meanwhile, graphene armor plays a key role in

sustaining vacancy sites without rapid deterioration (Fig. S33, ESI†).

Cryo-transmission electron microscopy (Cryo-TEM) was employed to further inspect the microstructure of SEI.[48] As illustrated in Fig. 5a, a myriad of crystal domains could be witnessed in the SEI formed by Al_2O_3@mG, implying the richness of inorganic components. In response, the crystalline region mainly consists of Li_3N, Li_2O, Li_2S, Li_2CO_3 and LiF, as evidenced by the corresponding FFT patterns (Fig. 5b–f).[49] In particular, the marked areas 1, 4 and 5 can be indexed to the (111) planes of Li_3N, LiF and Li_2S, respectively.[50] It is hence concluded that the SEI formed *via* Al_2O_3@mG is composed of many inorganic components derived from the decomposition of TFSI anions, validating the favorable SEI formation mediated by such a vacancy sustainer (Fig. 5g). In stark contrast, the SEI formed by bare Al_2O_3 is quite amorphous, in which Li_2CO_3 becomes the main component instead of LiF and Li_3N (Fig. 5h–j). The proportion of organic components is also increased owing to dominant solvent decomposition, leading to an inhomogeneous thick SEI layer (Fig. 5k).

To clarify the mechanism of V_O-mediated SEI formation, the adsorption energies between anions and Al_2O_3@mG were subject to DFT calculations (Fig. 5l).[51] Although adsorption configurations are similar, the introduction of V_O into Al_2O_3 enhances the capture of $TFSI^-$ with the adsorption energy augmenting from 0.69 eV to 4.10 eV (Fig. 5m). Likewise, the adsorption between NO_3^- and Al_2O_3@mG is also stronger than that for bare Al_2O_3, which promotes the breaking of N–O bonds (Fig. S34, ESI†). In terms of lithiophilicity, the adsorption configurations of Li^+ on the Al-top site, O-top site and near O vacancy-top site were taken into consideration (Fig. S35 and S36, ESI†).[52] Among them, Li^+ near the O vacancy-top site affords a lower adsorption energy (−1.58 eV) than those of other configurations, confirming that Al_2O_3 with oxygen vacancies would exhibit stronger affinity with Li^+. Moreover, the diffusion pathways of Li^+ on Al_2O_3@mG and Al_2O_3 were investigated (Fig. S37, ESI†). In this respect, the apparently lower energy barrier for Al_2O_3@mG manifests that V_O and graphene chainmail boost ion transport and facilitates interfacial kinetics (Fig. S38, ESI†). Finite element method simulations of the spatial Li^+ distributions were performed to reveal the ion flux status over the Li electrode. In general, the reverse migration and accumulation of anions in the electrolyte deteriorate Li^+ transport under a continuously applied electric field.[53] The imbalance between Li^+ consumption and transport would result in a depletion of Li^+ near the anode surface. Encouragingly, Al_2O_3@mG helps boost the concentration of Li^+ near the surface of Li anode, thereby enhancing interfacial charge transfer and homogenizing lithium deposition (Fig. 5n and Fig. S39, S40, ESI†).

Electrochemical performance

To comprehensively probe the electrochemical performances, coin-type Li–S batteries were assembled with Al_2O_3@mG or Al_2O_3 modified separators. Fig. 6a presents the CV profiles of full batteries within a voltage window of 1.7–2.8 V at a scan rate
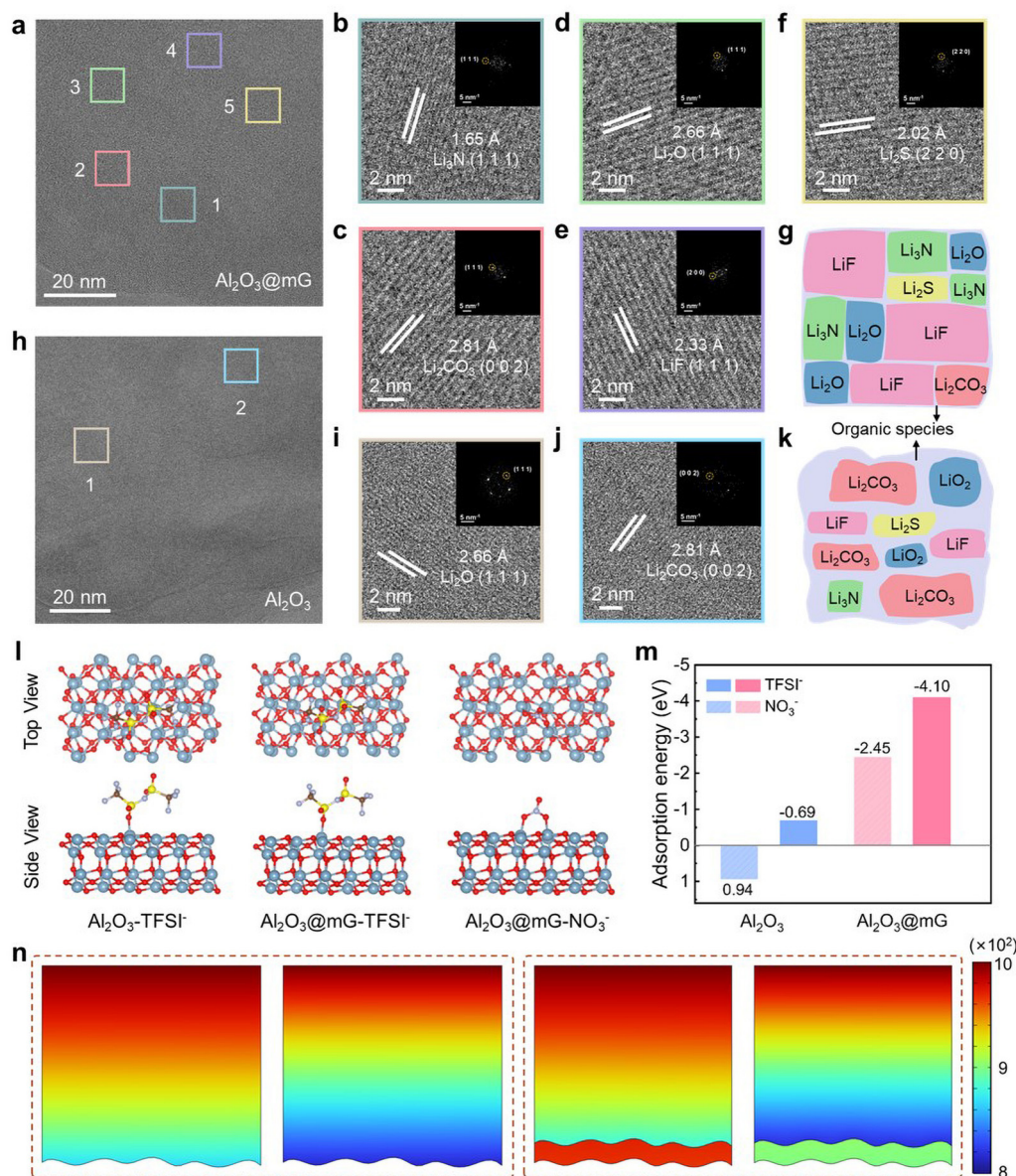
5946 | *Energy Environ. Sci.*, 2025, **18**, 5940–5951

This journal is © The Royal Society of Chemistry 2025

Fig. 5 Compositional analysis and mechanistic investigation of SEI. (a) Cryo-TEM images of the SEI formed by Al$_2$O$_3$@mG. (b)−(f) Representative HRTEM images showing (b) Li$_3$N, (c) Li$_2$CO$_3$, (d) Li$_2$O, (e) LiF, and (f) Li$_2$S phases from region 1–5. (g) Schematic of the SEI formed by Al$_2$O$_3$@mG. (h) Cryo-TEM images of the SEI formed by Al$_2$O$_3$. (i) and (j) Representative HRTEM images of (i) Li$_2$O and (j) Li$_2$CO$_3$ phases from region 1, 2. (k) Schematic of the SEI formed by Al$_2$O$_3$. (l) Adsorption structures of TFSI$^-$ and NO$_3^-$ on Al$_2$O$_3$ and Al$_2$O$_3$@mG. (m) Corresponding adsorption energies. (n) Finite element method simulations of the spatial Li$^+$ distributions of Al$_2$O$_3$ (left panels) and Al$_2$O$_3$@mG (right panels).

of 0.05 mV s^{-1}. Two featured reduction peaks (peak i and peak ii) appear at 2.3–2.4 V and 1.9–2.1 V during the discharge process, corresponding to the formation of soluble polysulfides and insoluble Li$_2$S, respectively. Meanwhile, the oxidation peaks are contributed by the Li$_2$S decomposition during the charge process. Note that the Al$_2$O$_3$@mG/PP exhibits a higher current response and smaller voltage polarization among the tested systems, indicative of robust electrocatalytic activity toward the sulfur redox reactions. The as-derived Tafel slopes of both reduction and oxidation peaks were used to quantify the electrocatalytic activity.[54] With respect to peak ii, the slope values for Al$_2$O$_3$@mG/PP, Al$_2$O$_3$/PP, and PP reach 25.0, 28.1,

and 39.6 mV dec^{-1}, respectively (Fig. S41, ESI†). As for the peak iii ascribed to Li$_2$S dissociation, Al$_2$O$_3$@mG/PP also exhibits a smaller Tafel slope, suggesting a kinetically favorable sulfur reaction. Furthermore, CV curves at scan rates ranging from 0.1 to 0.5 mV s^{-1} were collected to investigate the Li-ion diffusion based on the Randles–Sevcik equation (Fig. S42, ESI†). The fitted curve for Al$_2$O$_3$@mG/PP is much sharper, signifying optimized Li-ion migration and improved reaction kinetics under the regulation of V$_O$ and graphene chainmail (Fig. S43, ESI†). As demonstrated by electrochemical impedance spectroscopy (EIS) analysis, the Al$_2$O$_3$@mG/PP shows smaller values for both R_1 (equivalent series resistance) and R_{ct} (charge-
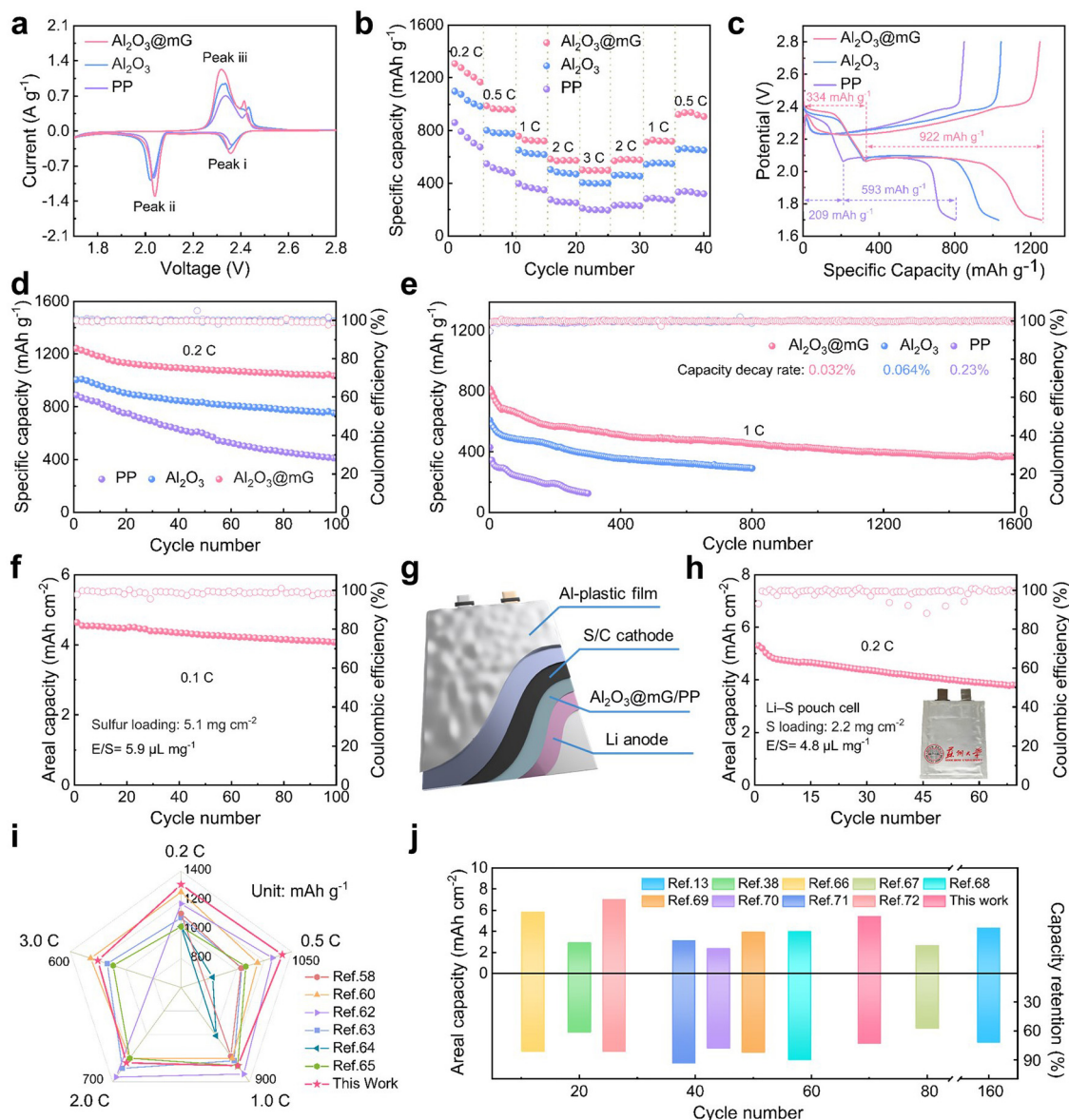
This journal is © The Royal Society of Chemistry 2025

Energy Environ. Sci., 2025, **18**, 5940–5951 | **5947**

Fig. 6 Electrochemical performance. (a) CV profiles of Li−S batteries with Al$_2$O$_3$@mG/PP, Al$_2$O$_3$/PP, and PP separators at 0.05 mV s^{-1}. (b) Rate performances. (c) GCD profiles at 0.2 C. (d) and (e) Cycling performances at 0.2 C and 1.0 C, respectively. (f) Cyclic performances of Li−S batteries equipped with Al$_2$O$_3$@mG modified separators with a sulfur loading of 5.1 mg cm^{-2}. (g) Schematic of the pouch cell equipped with the Al$_2$O$_3$@mG modified separator. (h) Cycling performance of an assembled pouch cell at 0.2 C. Comparison of (i) the coin cell and (j) the pouch cell between this work and related counterparts in Li−S batteries.

transfer resistance),[55] which can be attributed to the high electrical conductivity and fast interfacial reaction (Fig. S44, ESI†).

Rate performances of Al$_2$O$_3$@mG/PP, Al$_2$O$_3$/PP and PP were evaluated under different current densities (Fig. 6b). Al$_2$O$_3$@mG/PP demonstrates an obvious advantage, delivering capacities of 1307.5, 998.4, 772.9, 611.2, and 515.6 mA h g^{-1} at 0.2, 0.5, 1.0, 2.0 and 3.0 C, respectively. When the current density is switched back to 0.5 C, a capacity of 948.6 mA h g^{-1} could be recovered. Even at a high rate of 3.0 C, Al$_2$O$_3$@mG/PP enables two obvious discharge plateaus (Fig. S45, ESI†), indicative of efficient reaction kinetics. Alongside, galvanostatic

charge/discharge (GCD) profiles at 0.2 C were collected (Fig. 6c). Notably, Al$_2$O$_3$@mG/PP not only delivers a higher capacity but also exhibits a lower voltage gap in comparison with its other counterparts, again confirming the kinetically favorable polysulfide conversion as well as reduced reaction polarization. The corresponding discharge capacities at high-voltage and low-voltage plateaus are shown in Fig. S46 (ESI†), where the Al$_2$O$_3$@mG/PP presents the larger values of 334 and 922 mA h g^{-1}, respectively. As shown in Fig. 6d, the Al$_2$O$_3$@mG/ PP harvests a high initial capacity with a favorable capacity retention after 100 cycles at 0.2 C, which is also superior to that of Al$_2$O$_3$/PP and PP.

5948 | Energy Environ. Sci., 2025, **18**, 5940–5951

This journal is © The Royal Society of Chemistry 2025

When the current density is increased to 1.0 C, it is still able to achieve a reversible capacity of 374.2 mA h g^{-1} with a low decay rate of 0.032% per cycle after 1600 cycles, verifying the versatile functions of Al$_2$O$_3$@mG in restraining polysulfide shuttling and improving sulfur utilization (Fig. 6e). As presented in Fig. S47 (ESI†), Li–S batteries with an elevated sulfur loading and low electrolyte usage were also assembled. With a sulfur loading of 3.1 and 4.2 mg cm^{-2}, they are able to operate stably for 40 cycles at 0.1 C, respectively yielding a maximum areal capacity of 3.9 and 4.1 mA h cm^{-2}. More encouragingly, the Al$_2$O$_3$@mG/PP delivers an areal capacity of 4.7 mA h cm^{-2} at a sulfur loading of 5.1 mg cm^{-2}, exceeding that of commercial Li-ion batteries (Fig. 6f and Table S2, ESI†).[56–61] To further explore its practical potential, pouch cells with a thin Li anode (50 μm) and an *E/S* ratio of 4.8 μL mg^{-1} were assembled (Fig. 6g). With the aid of the Al$_2$O$_3$@mG modified separator, it realizes an initial areal capacity of 5.4 mA h cm^{-2}, accompanied by a capacity retention of 73.1% at 0.2 C over 70 cycles (Fig. 6h). As shown in galvanostatic charge/discharge curves of a Li–S pouch cell, two typical discharge plateaus can be clearly observed (Fig. S48, ESI†), demonstrating a kinetically favorable sulfur reaction. Benefiting from such a dual-functional mediator and vacancy catalysis sustainer, the performances of Li–S batteries equipped with Al$_2$O$_3$@mG compare favorably with their related counterparts in both coin-type and pouch-cell configurations (Fig. 6i and j and Table S3, ESI†).[13,38,58,60,62–72]

Conclusions

We have designed a dual-functional V$_O$-rich Al$_2$O$_3$ mediator for Li–S batteries, which was encapsulated by graphene chainmail with controlled layer number *via* the CVD technique. It is revealed that the electrocatalytically active sites of Al$_2$O$_3$ with a moderate vacancy concentration can be maintained with the aid of a tailored multi-layer graphene armor, which functions as a catalysis sustainer to mitigate the detrimental coverage of insulating discharge product and promote catalytic durability. Meanwhile, V$_O$-rich Al$_2$O$_3$@mG is conducive to inducing homogeneous Li deposition and promoting the preferential decomposition of anions, thereby rendering a stable inorganic-rich SEI layer and inhibiting Li dendrite growth. Consequently, Li–S batteries equipped with Al$_2$O$_3$@mG modified separators exhibit impressive cycling stability with a low capacity decay rate at 0.032% per cycle after 1600 cycles at 1.0 C. The assembled pouch cells with a thin Li anode and a low *E/S* ratio acquire a high areal capacity with stable operation over 70 cycles. Our work explores the maintenance mechanism of vacancies and their role in mediating electrolyte decomposition as well as SEI generation, which opens an avenue for the rational modulation of dual-functional mediators toward Li–S commercialization.

Author contributions

J. Sun conceived the idea. J. Gu, Y. Wu and Y. Song performed the synthesis of a dual-functional mediator. J. Gu, Y. Wu, Z. Chen and M. Lu carried out the material characterization and electrochemical measurements. Y. Mu, H. Gu and L. Zeng carried out the cryo-TEM measurements. M. Tian and K. Chen conducted the computational simulations. The manuscript was written by J. Gu, Z. Shi, Q. Zhang and J. Sun with input from all authors. All authors contributed to the analysis and discussion of the results leading to the manuscript. All authors have given approval to the final version of the manuscript.

Data availability

The data supporting this article have been included as part of the ESI.†

Conflicts of interest

The authors declare no competing interests.

Acknowledgements

References

1 S. Chung and A. Manthiram, *Adv. Mater.*, 2019, **31**, 1901125.
2 P. Bruce, S. Freunberger, L. Hardwick and J. Tarascon, *Nat. Mater.*, 2011, **11**, 19.
3 Z. Shi, M. Li, J. Sun and Z. Chen, *Adv. Energy Mater.*, 2021, **11**, 2100332.
4 D. Liu, C. Zhang, G. Zhou, W. Lv, G. Ling, L. Zhi and Q. Yang, *Adv. Sci.*, 2017, **5**, 1700270.
5 Z. Shi, Y. Ding, Q. Zhang and J. Sun, *Adv. Energy Mater.*, 2022, **11**, 2100332.
6 C. Ye, Y. Jiao, H. Jin, A. Slattery, K. Davey, H. Wang and S. Qiao, *Angew. Chem., Int. Ed.*, 2018, **57**, 16703.
7 M. Jana, R. Xu, X. Cheng, J. S. Yeon, J. M. Park, J. Huang, Q. Zhang and H. S. Park, *Energy Environ. Sci.*, 2020, **13**, 1049.
8 A. Hu, M. Zhou, T. Lei, Y. Hu, X. Du, C. Gong, C. Shu, J. Long, J. Zhu, W. Chen, X. Wang and J. Xiong, *Adv. Energy Mater.*, 2020, **10**, 2002180.
9 Y. Ding, Q. Cheng, J. Wu, T. Yan, Z. Shi, M. Wang, D. Yang, P. Wang, L. Zhang and J. Sun, *Adv. Mater.*, 2022, **34**, 2202256.
10 Z. Shi, Z. Tian, D. Guo, Y. Wang, Z. Bayhan, A. Alzahrani and H. Alshareef, *ACS Energy Lett.*, 2023, **8**, 3054.
11 Q. Ran, J. Liu, L. Li, Q. Hu, H. Zhao, S. Komarneni and X. Liu, *Adv. Funct. Mater.*, 2024, **34**, 2402872.
12 S. Zhai, Z. Ye, R. Liu, H. Xu, C. Li, W. Liu, X. Wang and T. Mei, *Adv. Funct. Mater.*, 2023, **34**, 2314379.
13 L. Chen, Y. Sun, X. Wei, L. Song, G. Tao, X. Cao, D. Wang, G. Zhou and Y. Song, *Adv. Mater.*, 2023, **35**, 2300771.

This journal is © The Royal Society of Chemistry 2025

Energy Environ. Sci., 2025, **18**, 5940–5951 | 5949

14 R. Razaq, M. M. U. Din, D. R. Småbråten, V. Eyupoglu, S. Janakiram, T. O. Sunde, N. Allahgoli, D. Rettenwander and L. Deng, *Adv. Energy Mater.*, 2023, **14**, 2302897.

15 Y. Zhang, Y. Qiu, L. Fan, X. Sun, B. Jiang, M. Wang, X. Wu, D. Tian, X. Song, X. Yin, Y. Shuai and N. Zhang, *Energy Storage Mater.*, 2023, **63**, 103026.

16 M. Wang, Z. Sun, H. Ci, Z. Shi, L. Shen, C. Wei, Y. Ding, X. Yang and J. Sun, *Angew. Chem., Int. Ed.*, 2021, **60**, 24558–24565.

17 H. Li, R. Gao, B. Chen, C. Zhou, F. Shao, H. Wei, Z. Han, N. Hu and G. Zhou, *Nano Lett.*, 2022, **22**, 4999.

18 Y. Shi, D. Zhang, H. Miao, X. Wu, Z. Wang, T. Zhan, J. Lai and L. Wang, *Sci. China Chem.*, 2022, **65**, 1829.

19 Z. Shi, Z. Sun, J. Cai, X. Yang, C. Wei, M. Wang, Y. Ding and J. Sun, *Adv. Mater.*, 2021, **33**, 2103050.

20 C. Zhao, B. Jiang, Y. Huang, X. Sun, M. Wang, Y. Zhang and N. Zhang, *Energy Environ. Sci.*, 2023, **16**, 5490.

21 R. Wang, C. Luo, T. Wang, G. Zhou, Y. Deng, Y. He, Q. Zhang, F. Kang, W. Lv and Q. H. Yang, *Adv. Mater.*, 2020, **32**, 2000315.

22 J. He, A. Bhargav and A. Manthiram, *ACS Nano*, 2021, **15**, 8583.

23 J. Gu, Z. Shi, T. Yan, M. Tian, Z. Chen, S. Chen, Y. Ding, M. Lu, Y. Zou, J. Zhang, L. Zhang and J. Sun, *Small*, 2024, **21**, 2407196.

24 J. Cai, Z. Sun, W. Cai, N. Wei, Y. Fan, Z. Liu, Q. Zhang and J. Sun, *Adv. Funct. Mater.*, 2021, **31**, 2100586.

25 H. Ci, J. Cai, H. Ma, Z. Shi, G. Cui, M. Wang, J. Jin, N. Wei, C. Lu, W. Zhao, J. Sun and Z. Liu, *ACS Nano*, 2020, **14**, 11929.

26 P. Liu, H. Hao, A. Singla, B. Vishnugopi, J. Watt, P. Mukherjee and D. Mitlin, *Angew. Chem., Int. Ed.*, 2024, **63**, 202402214.

27 M. Wang, Y. Song, N. Wei, Y. Shao, G. Sheng and J. Sun, *Chem. Eng. J.*, 2021, **418**, 129407.

28 M. Wang, Y. Zhu, Y. Sun, Y. Zhao, X. Yang, X. Wang, Y. Song, H. Ci and J. Sun, *Adv. Funct. Mater.*, 2022, **33**, 2211978.

29 Y. Tian, G. Li, Y. Zhang, D. Luo, X. Wang, Y. Zhao, H. Liu, P. Ji, X. Du, J. Li and Z. Chen, *Adv. Mater.*, 2020, **32**, e1904876.

30 P. Wang, J. Bao, K. Lv, N. Zhang, Z. Chang, P. He and H. Zhou, *ACS Appl. Mater. Interfaces*, 2019, **11**, 35788–35795.

31 N. Wang, B. Chen, K. Qin, E. Liu, C. Shi, C. He and N. Zhao, *Nano Energy*, 2019, **60**, 332.

32 B. Q. Li, L. Kong, C. X. Zhao, Q. Jin, X. Chen, H. J. Peng, J. L. Qin, J. X. Chen, H. Yuan, Q. Zhang and J. Q. Huang, *InfoMat*, 2019, **1**, 533.

33 C. Zhao, Y. Huang, B. Jiang, Z. Chen, X. Yu, X. Sun, H. Zhou, Y. Zhang and N. Zhang, *Adv. Energy Mater.*, 2023, **14**, 2302586.

34 M. Lu, T. Yan, Y. Ding, S. Chen, Z. Chen, J. Gu, X. Chen, L. Zhang, M. Tian and J. Sun, *Energy Storage Mater.*, 2024, **70**, 103458.

35 A. Thompson, H. Aktulga, R. Berger, D. Bolintineanu, W. Brown, P. Crozier, P. In't Veld, A. Kohlmeyer, S. Moore, T. Nguyen, R. Shan, M. Stevens, J. Tranchida, C. Trott and S. Plimpton, *Comput. Phys. Commun.*, 2022, **271**, 108171.

36 P. Xiong, F. Zhang, X. Zhang, Y. Liu, Y. Wu, S. Wang, J. Safaei, B. Sun, R. Ma, Z. Liu, Y. Bando, T. Sasaki, X. Wang, J. Zhu and G. Wang, *Nat. Commun.*, 2021, **12**, 4184.

37 J. Cai, J. Jin, Z. Fan, C. Li, Z. Shi, J. Sun and Z. Liu, *Adv. Mater.*, 2020, **32**, 2005967.

38 Y. Kong, L. Wang, M. Mamoor, B. Wang, G. Qu, Z. Jing, Y. Pang, F. Wang, X. Yang, D. Wang and L. Xu, *Adv. Mater.*, 2024, **36**, 2310143.

39 Y. Li, Z. Chen, X. Y. Zhong, T. Mei, Z. Li, L. Yue, J. L. Yang, H. J. Fan and M. Xu, *Adv. Funct. Mater.*, 2024, **35**, 2412279.

40 J. Wang, S. Yi, J. Liu, S. Sun, Y. Liu, D. Yang, K. Xi, G. Gao, A. Abdelkader, W. Yan, S. Ding and R. V. Kumar, *ACS Nano*, 2020, **14**, 9819.

41 W. Yao, J. Xu, L. Ma, X. Lu, D. Luo, J. Qian, L. Zhan, I. Manke, C. Yang, P. Adelhelm and R. Chen, *Adv. Mater.*, 2023, **35**, 2212116.

42 Q. Zhao, S. Stalin and L. A. Archer, *Joule*, 2021, **5**, 1119.

43 P. Zhai, Q. He, H. Jiang, B. Gao, B. Zhang, Q. Chen, Z. Yang, T. Wang and Y. Gong, *Adv. Energy Mater.*, 2023, **14**, 2302730.

44 X. Lian, Z. Ju, L. Li, Y. Yi, J. Zhou, Z. Chen, Y. Zhao, Z. Tian, Y. Su, Z. Xue, X. Chen, Y. Ding, X. Tao and J. Sun, *Adv. Mater.*, 2024, **36**, 2306992.

45 X. Wang, Z. Chen, X. Xue, J. Wang, Y. Wang, D. Bresser, X. Liu, M. Chen and S. Passerini, *Nano Energy*, 2025, **133**, 110439.

46 S. Ni, M. Zhang, C. Li, R. Gao, J. Sheng, X. Wu and G. Zhou, *Adv. Mater.*, 2023, **35**, 2209028.

47 C. Bi, N. Yao, X. Li, Q. Zhang, X. Chen, X. Zhang, B. Q. Li and J. Huang, *Adv. Mater.*, 2024, **36**, 2411197.

48 Y. Mu, S. Yu, Y. Chen, Y. Chu, B. Wu, Q. Zhang, B. Guo, L. Zou, R. Zhang, F. Yu, M. Han, M. Lin, J. Yang, J. Bai and L. Zeng, *Nano-Micro Lett.*, 2024, **16**, 86.

49 X. Cheng, S. Yang, Z. Liu, J. X. Guo, F. Jiang, F. Jiang, X. Xiong, W. Tang, H. Yuan, J. Huang, Y. Wu and Q. Zhang, *Adv. Mater.*, 2024, **36**, e2307370.

50 Y. Mu, Y. Chu, Y. Shi, C. Huang, L. Yang, Q. Zhang, C. Li, Y. Feng, Y. Zhou, M. Han, T. Zhao and L. Zeng, *Adv. Energy Mater.*, 2024, **14**, 2400725.

51 B. Xu, L. Ma, W. Wang, H. Zhu, Y. Zhang, C. Liang, L. Zhou, L. Wang, Y. Zhang, L. Chen, C. Zhang and W. Wei, *Adv. Mater.*, 2024, **36**, 2311938.

52 J. Qin, F. Pei, R. Wang, L. Wu, Y. Han, P. Xiao, Y. Shen, L. Yuan, Y. Huang and D. Wang, *Adv. Mater.*, 2024, **36**, e2312773.

53 R. Xu, Y. Xiao, R. Zhang, X. Cheng, C. Z. Zhao, X. Zhang, C. Yan, Q. Zhang and J. Huang, *Adv. Mater.*, 2019, **31**, 1808392.

54 B. Jiang, C. Zhao, X. Yin, Y. Zhang, X. Sun, S. Gu and N. Zhang, *Energy Storage Mater.*, 2024, **66**, 103237.

55 J. Sun, Y. Sun, M. Pasta, G. Zhou, Y. Li, W. Liu, F. Xiong and Y. Cui, *Adv. Mater.*, 2016, **28**, 9797.

56 Z. Li, J. Zhang and X. W. Lou, *Angew. Chem., Int. Ed.*, 2015, **54**, 12886.

57 A. Joshi, T. S. Anand, J. Kala, M. Singh, A. Gupta, R. K. Srivastava and B. Nandan, *ACS Appl. Energ. Mater.*, 2023, 7, 312.

58 T. Sun, X. Zhao, B. Li, H. Shu, L. Luo, W. Xia, M. Chen, P. Zeng, X. Yang, P. Gao, Y. Pei and X. Wang, *Adv. Funct. Mater.*, 2021, **31**, 2101285.

5950 | *Energy Environ. Sci.*, 2025, **18**, 5940–5951

This journal is © The Royal Society of Chemistry 2025

59 P. Guo, P. Jiang, W. Chen, G. Qian, D. He and X. Lu, *Electrochim. Acta*, 2022, **428**, 140955.

60 J. Xia, R. Gao, Y. Yang, Z. Tao, Z. Han, S. Zhang, Y. Xing, P. Yang, X. Lu and G. Zhou, *ACS Nano*, 2022, **16**, 19133.

61 H. Park, S. Lee, H. Kim, H. Park, H. Kim, J. Kim, M. Agostini, Y. K. Sun and J. Y. Hwang, *Carbon Energy*, 2024 **6**, 472.

62 D. Cai, J. Yang, T. Liu, S. Zhao and G. Cao, *Nano Energy*, 2021, **89**, 106452.

63 Z. Fang, J. Tan, L. Ma, P. Yi, W. Lu, Y. Xu, M. Ye and J. Shen, *Nanoscale*, 2024, **16**, 17934.

64 P. Geng, Y. Lin, M. Du, C. Wu, T. Luo, Y. Peng, L. Wang, X. Jiang, S. Wang, X. Zhang, L. Ni, S. Chen, M. Shakouri and H. Pang, *Adv. Sci.*, 2023, **10**, 2302215.

65 Y. Wang, H. Wang, Y. Jiang, G. Li, S. Liu and X. Gao, *ACS Appl. Energy Mater.*, 2023, **6**, 8377.

66 H. Cheng, S. Zhang, S. Li, C. Gao, S. Zhao, Y. Lu and M. Wang, *Small*, 2022, **18**, 2202557.

67 M. Kim, M. Kim, V. Do, Y. Xia, W. Kim and W. I. Cho, *J. Power Sources*, 2019, **422**, 104.

68 L. Luo, S. H. Chung, H. Yaghoobnejad Asl and A. Manthiram, *Adv. Mater.*, 2018, **30**, 1804149.

69 L. Luo, J. Li, H. Yaghoobnejad Asl and A. Manthiram, *ACS Energy Lett.*, 2020, **5**, 1177.

70 R. Yang, F. Wang, W. Cui, W. Chen, T. Lei, D. Chen, D. CHen, X. Li, Z. Chi, C. Kai, D. Run, Y. Yi, N. Xiao and H. Yin, *Energy Storage Mater.*, 2025, **75**, 104030.

71 W. Yao, J. Xu, Y. Cao, Y. Meng, Z. Wu, L. Zhan, Y. Wang, Y. Zhang, I. Manke, N. Chen, C. Yang and R. Chen, *ACS Nano*, 2022, **16**, 10783.

72 X. Zhang, Q. Jin, Y. Nan, L. Hou, B. Q. Li, X. Chen, Z. H. Jin, X. Zhang, J. Huang and Q. Zhang, *Angew. Chem., Int. Ed.*, 2021, **60**, 15503.

This journal is © The Royal Society of Chemistry 2025

Energy Environ. Sci., 2025, **18**, 5940–5951 | **5951**